



**TECHNISCHE
UNIVERSITÄT
WIEN**
Vienna University of Technology

Diplomarbeit

Entanglement Entropy of a Compact Region in a $2D$ -Dilaton Gravity Theory

Ausgeführt am
Institut für Theoretische Physik
der Technischen Universität Wien

unter der Anleitung von
Assistant Prof. Dr.techn. Daniel Grumiller
und
Projektass.(FWF) Dipl.-Ing. Christian Ecker

durch
Ognen Kapetanoski
Matrikelnummer: 0828180
Freihofgasse 6-8/3
1190 Wien

Wien, am 09.05.2016

Abstract

The two-point function and the entanglement entropy can be seen as quantities to describe properties of the quark-gluon plasma. For this an anisotropic 5-dimensional system is considered.

A homogeneous anisotropic but $O(2)$ symmetric solution to the 5-dimensional vacuum Einstein equations is equivalent to a homogeneous and isotropic solution to the Einstein equations including a scalar field. The corresponding 5-dimensional Einstein-Hilbert action without scalar field can be dimensionally reduced to a 2-dimensional dilaton gravity action with two scalar fields. The same 2-dimensional dilaton gravity action arises from reducing isotropic Einstein gravity with a minimally coupled massless scalar field. Therefore, the 2-dimensional dilaton gravity is equivalent to the 5-dimensional anisotropic system with matter and the 5-dimensional isotropic system with a scalar field.

In this thesis the two-point function of operators of large conformal weight and the holographic entanglement entropy for a spherical region in a 2-dimensional dilaton gravity theory are calculated numerically using the Anti-de Sitter/conformal field theory correspondence. The two-point function, which is computed in the geodesic approximation, amounts to a geodesic's length in the gravity theory. Similarly the calculation of the entanglement entropy reduces to finding geodesics in an auxiliary spacetime.

To obtain the geometry the Einstein equations need to be solved numerically. The Einstein equations of the 2-dimensional dilaton gravity theory are mapped to the vacuum Einstein equations for an anisotropic geometry.

The numerical calculation of geodesics is performed using a Mathematica package, which calculates the geodesics with a relaxation method. The results for the entanglement entropy and two-point function vary strongly, depending on the chosen boundary region.

CONTENTS

Contents

1	Introduction	1
2	Background	3
2.1	Entanglement entropy	3
2.2	Heavy ion collisions and quark-gluon plasma	4
2.3	AdS/CFT correspondence	6
2.4	$\mathcal{N} = 4$ SYM plasma as toymodel for QGP in HIC	7
2.5	Holographic calculation of entanglement entropy	8
2.6	Einstein equations	9
3	Geometry	11
3.1	2-dimensional dilaton gravity	11
3.2	The map from anisotropic AdS_5 to isotropic AdS_5	12
3.3	Numerical approach to the Einstein equations	12
4	The two point function and entanglement entropy for a spherical region	17
4.1	Two-point functions	17
4.2	Holographic entanglement entropy for a spherical region from geodesics	18
4.3	Calculating the geodesic	19
5	Numerical results	21
5.1	Time evolution of the two-point function	22
5.2	Time evolution of the entanglement entropy	24
6	Conclusion and outlook	27
6.1	Conclusion	27
6.2	Outlook	28
A	Eddington-Finkelstein coordinates	29
B	Parametrising the spherical region	29

1 Introduction

Today, one of the primary objectives of physicists is to find a theory that merges all branches of physics. Therefore many theories have been considered to explain how the universe works and describe all physical phenomena with one language.

The quark-gluon plasma (QGP) is an exceptional matter form that can not be obtained under normal conditions. Here the quarks and gluons are no longer confined to hadrons above a characteristic energy scale. The QGP state can be achieved in nuclear physics, where the characteristic energy scale is reached by collisions of heavy (gold and lead) ions at nearly the speed of light (see section 2.2). Our enthusiasm in this matter is based on the assumption, that in the early stages of the universe matter existed at high energies, corresponding to the QGP. Numerical calculations in order to simulate this matter are not possible in perturbative quantum chromodynamics (QCD). Therefore in the interest of describing the QGP other methods are needed.

One promising approach is provided by the holographic principle, namely the Anti-de Sitter/conformal field theory (AdS/CFT) correspondence described in 2.3. This establishes a duality between gauge and gravity theories. Looking at the quantum field theory (QFT), it is typical to examine how the correlation functions of local operators behave. Other quantities, such as the energy density are also observed. In this context we are interested in the two-point function (2PF) and the entanglement entropy (EE).

The EE and the 2PF represent quantities, with which the QGP can be partially described. As shown in chapter (4), the computation of the 2PF and the EE reduces to solving the geodesic equations. In order to do this, the metric is needed, which we obtain by solving the Einstein equations. Since there is no analytical solution for the case that we are interested in, numerical algorithms in Octave [1] and Mathematica [2] are used.

In this thesis we start with chapter 2 by introducing the framework that will be used later on. This includes several topics: the entanglement entropy, the heavy ion collisions (HIC) in the high energy physics, the AdS/CFT field theory correspondence using holography, the $\mathcal{N} = 4$ supersymmetric Yang-Mills theory describing plasma, followed by the holographic calculation of the entanglement entropy and the Einstein equations. Chapter 3 considers the applied geometry, starting from the 2-dimensional dilaton gravity, maps for the entanglement entropy and the two-point function between anisotropic and isotropic AdS_5 , and the numerical solution of the Einstein equations. The following chapter 4 goes into detail regarding the connection of the 2PF and the EE with the geodesic. The numerical results of the time evolution of these two observables are presented in chapter 5. At the end in chapter 6 the conclusion and outlook are presented. In appendix A one can find the transformation to the Eddington-Finkelstein coordinates, while in appendix B the parametrising to a spherical region is mathematically described.

2 Background

In this thesis we calculate the entanglement entropy and the two-point function in a 2-dimensional dilaton gravity with scalar matter. First we define these quantities and bring motivation for why we are considering them, namely the heavy ion collisions (HICs). Further the concepts of the AdS/CFT correspondence are discussed.

2.1 Entanglement entropy

One of the many motivations to study EE is condensed matter physics. The EE can be used as an order parameter to study quantum phase transitions. In the following the basic ideas and properties of the entanglement entropy are presented [3].

Definition of entanglement entropy

Entanglement entropy is a measure for the entanglement in a quantum system. Let us consider such a system at zero temperature in the pure non-degenerate ground state. The density matrix of the total system is given by

$$\rho_{tot} = |\Psi\rangle \langle\Psi|, \quad (2.1)$$

and the von Neumann entropy is zero,

$$S_{tot} = -\text{tr}(\rho_{tot} \log(\rho_{tot})) = 0. \quad (2.2)$$

Next divide the system into two disjoint regions A and B as shown in Figure 1. The

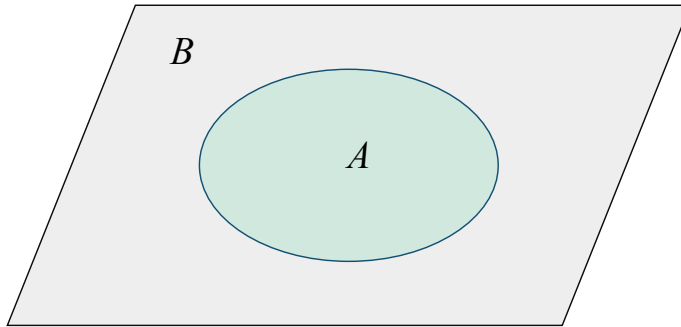


Figure 1: The system being divided into two subsystems A and B .

total Hilbert space becomes a direct product $\mathcal{H}_{tot} = \mathcal{H}_A \otimes \mathcal{H}_B$, where \mathcal{H}_A and \mathcal{H}_B are the Hilbert spaces for region A and B respectively. An observer with access only to A can measure only the reduced density matrix

$$\rho_A = \text{Tr}_B \rho_{tot}, \quad (2.3)$$

where Tr_B denotes the trace only over the partial Hilbert space \mathcal{H}_B .

The entanglement entropy of the region A is defined as the von Neumann entropy of the reduced density matrix

$$S_A = -\text{Tr}_A [\rho_A \log(\rho_A)]. \quad (2.4)$$

Due to the expression (2.2) for the von Neumann entropy, in the case of time-dependency the density matrices ρ_{tot} and ρ_A become also time dependent. This is resolved by fixing a time t_0 when the entanglement entropy is measured.

Entanglement entropy in conformal field theory

Computing entanglement entropy in quantum field theories is in general very complicated. The basic method here is the replica method, which gives analytic results in $(1 + 1)$ -dimensional conformal field theory (CFT) [4].

On the CFT side, the EE for 2-dimensional CFT is analytically computed via [5, 4]

$$S_A = \frac{c}{6} \mathcal{A} \log \left(\frac{\xi}{a} \right), \quad (2.5)$$

where c is the central charge of the CFT, \mathcal{A} is the number of the boundary points of A , ξ is the correlation length and a is the ultra violet (UV) cutoff. In two dimensions $\mathcal{A} = 2$, which gives

$$S_A = \frac{c}{3} \log \left(\frac{\xi}{a} \right). \quad (2.6)$$

2.2 Heavy ion collisions and quark-gluon plasma

The system in which we want to calculate the EE are the heavy ion collisions (HIC), which are part of high energy physics. Particle accelerators have been extended to work up to temperatures of hundreds MeV and high energy densities. In these collisions gold nuclei with 197 nucleons (79 protons and 118 neutrons) at Relativistic Heavy Ion Collider (RHIC) and lead nuclei with 208 nucleons (82 protons and 126 neutrons) at the Large Hadron Collider (LHC) are used, providing large volumes of matter at a high energy density. The nuclei collide with velocities near the speed of light, which gives the total center of mass energy in such collision to be approximately 40 TeV at the RHIC and 600 TeV at the LHC. The tracks of the charged particles produced with lead ions performed at the LHC are shown in Figure 2. The multiplicities at LHC are around 5 times higher than at RHIC (due to larger energy densities [7, 8])¹. The particle multiplicities in collisions of gold and lead at different energies are shown in Figure 3.

The matter formed at this high temperature is explained with quarks and gluons, which are not confined into hadrons. The so called quark-gluon plasma (QGP) represents the deconfined state of strongly interacting matter, where quarks and gluons move freely within a larger volume instead of a nucleonic one [10]. Heavy ion collisions are an approach to study the QGP. Since the temperature of the QGP extends beyond $10^{12} K$ (nearly the temperature of the universe after the Big Bang²) [9] the HICs provide a way to investigate the state of matter that existed

¹At the LHC around 26000 particles can be generated [9].

²The Big Bang represents a cosmological model, explaining the early stages of the universe. This theory states that the universe began with a small singularity, and then started inflating over the next 16.8 billion years.

2 BACKGROUND

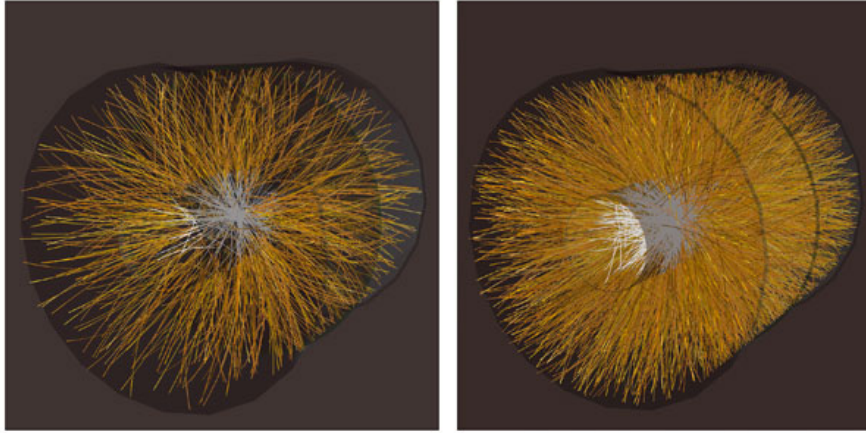


Figure 2: Tracks of charged particles from HICs registered by the ALICE detector at the LHC with lead nuclei. The tracks from few charged particles (low multiplicity, left) compared to the tracks of thousand of particles (high multiplicity, right) [6].

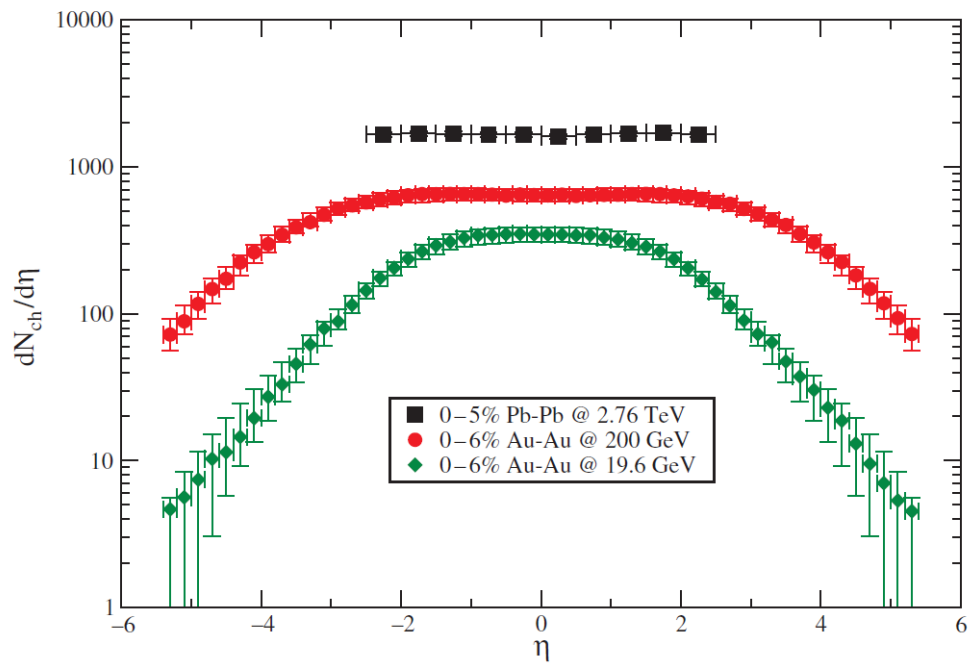


Figure 3: Charged particle multiplicity distributions for central collision [8]. Much higher energies are used at LHC for the lead collisions compared with the gold collisions at RHIC.

millionths of a second after the Big Bang. Initially QGP is highly out of equilibrium and thermalizes very fast to a hydrodynamic state (see Figure 4). It is important to consider that the QGP can be described with hydrodynamics at a specific time span. Research at RHIC and hydrodynamical calculations presume that the plasma's thermalization time is small $\tau_{therm} \lesssim 1 \text{ fm}/c$, which is roughly $3 \times 10^{-24} \text{ s}$ [11] (for more information see [10]).

Since the QGP is initially highly anisotropic, we consider an anisotropic system to study the thermalization process of the QGP. In this work a simple model is used in order to find observables that characterize the equilibration of the QGP.

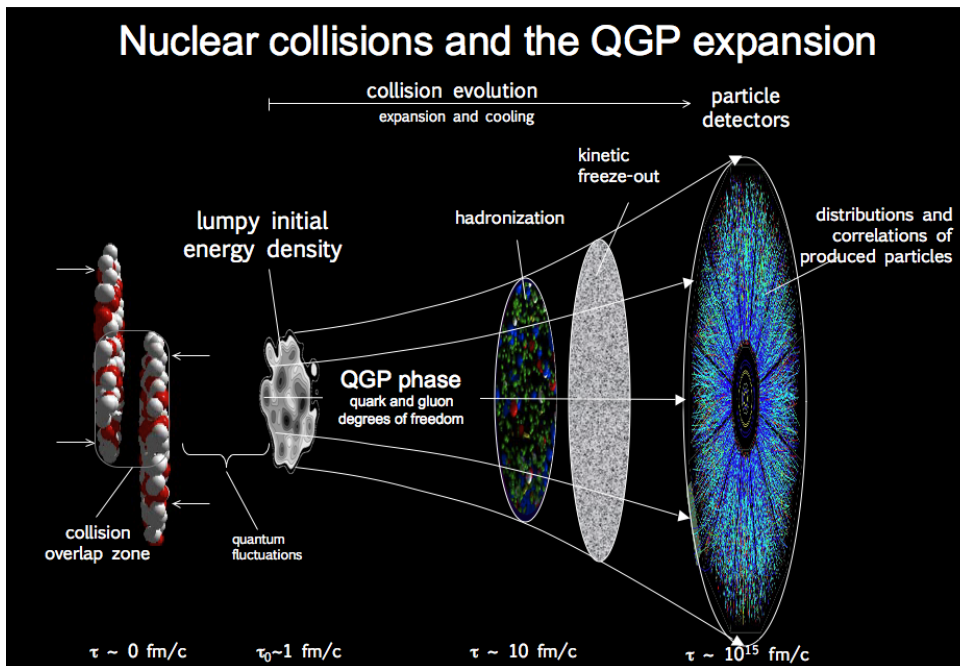


Figure 4: Illustration of the matter progression in relativistic heavy ion collisions. [12] .

It turns out that the QGP in these experiments is strongly coupled. For a large coupling constant, computations in a certain temperature span are not applicable in perturbative quantum chromodynamics (QCD). Computations can be done within lattice QCD, where the lattice-regularized calculations at non-zero temperature are performed with the imaginary time formalism. We are interested in the dynamics and the early state after the collision before the thermalisation of the QGP, where the lattice QCD approach/method fails. Furthermore the fermion sign problem prevents the usage of the Monte Carlo lattice simulations [8].

Due to these difficulties, different approaches have been introduced. The AdS/CFT correspondence turned out to be a useful additional tool in the QCD thermodynamic research.

2.3 AdS/CFT correspondence

The holographic principle provides a connection between a theory of quantum gravity defined in a d -dimensional spacetime and a quantum field theory without gravity

2 BACKGROUND

in one dimension lower, introduced by 't Hooft and Susskind [13, 14]. It states that all of the information enclosed in some region of space is represented as a hologram³ on the boundary of that region. This means that the information contained in both theories is equivalent.

The boundary of the Anti-de Sitter (AdS) space conformally corresponds to Minkowski's space. In that sense (the hologram) the quantum field theory (QFT) lies on the AdS boundary. A specific realization of the holographic principle is the AdS/CFT correspondence, stating the equivalence of $\mathcal{N} = 4$ supersymmetric Yang-Mills (SYM) theory with gauge group $SU(N_c)$ in 4 dimensions and Type *II B* string theory on $AdS_5 \otimes S^5$ [15]. Having in mind the holographic principle, the information in AdS_d space is embedded in the CFT_{d-1} . With this we can do calculations on one side and then translate them to the other side.

Due to this fact, the AdS/CFT correspondence is an interesting tool to study strongly coupled QFT using classical gravity on AdS. The limit which makes this possible is the limit of large N_c and large 't Hooft coupling $\lambda = N_c g^2$, where g is the coupling constant in the gauge theory. In this limit the string theory reduces to classical supergravity. This is a huge simplification, since the problem of solving a strongly coupled QFT can be replaced by the much easier task of solving classical general relativity.

In many fields the duality gives the opportunity to tackle problems that are not accessible by perturbation theory on the field theory side. For example the AdS/CFT correspondence is used in quantum gravity, particularly the black hole information paradox [16], and the field condensed matter physics of strongly correlated systems [17], where at quantum critical points the systems can be described with CFTs. The focus of this work are the applications of the AdS/CFT correspondence to high energy physics.

2.4 $\mathcal{N} = 4$ SYM plasma as toy model for QGP in HIC

The $\mathcal{N} = 4$ SYM plasma can be considered as a model for the QGP, due to the fact that both theories are similar at HIC energies.

Above a critical energy density $\epsilon_c \sim 1 \text{ GeV}/fm^3$ or critical temperature $T_c \sim 200 \text{ MeV}$ QCD is deconfined [10], while in $\mathcal{N} = 4$ SYM there is no confinement. $\mathcal{N} = 4$ SYM is a scale invariant theory, while scale invariance in QCD is broken by the running coupling constant. Above T_c although, this effect gets negligible and QCD is almost scale invariant too. The similarities in the confinement and scale invariance above T_c between these two theories motivate the assertion that QCD and $\mathcal{N} = 4$ SYM are comparable at non-zero temperatures (for detailed material refer to [8]).

We are interested in the early evolution (far from equilibrium) of the plasma state. There the shear viscosity over entropy density of the QGP is very small. This makes it an almost perfect fluid. Considering the AdS/CFT correspondence in the limits explained above, the shear viscosity is found to be $\eta/s = 1/4\pi$ [18].

³The hologram displays a three dimensional object represented in a two dimensional surface.

2.5 Holographic calculation of entanglement entropy

As discussed in 2.1 EE is hard to calculate in $d \geq 3$ using QFT-methods. Since we are interested in a 4-dimensional CFT, we approach this calculation holographically, where the AdS/CFT correspondence provides a simpler method that works also in higher dimensions. According to the Ryu-Takayanagi proposal [5, 19, 3], within AdS/CFT the holographic entanglement entropy (HEE) of a spatial region A in the field theory can be computed from the area \mathcal{A} of a surface in AdS_d spacetime

$$S_A = \frac{\mathcal{A}(\Sigma_A)}{4G_N^d}, \quad (2.7)$$

where Σ_A is a minimal surface which is attached to the boundary of the region A and G_N denotes the Newton constant in d dimensions. Figure 5 shows the minimal

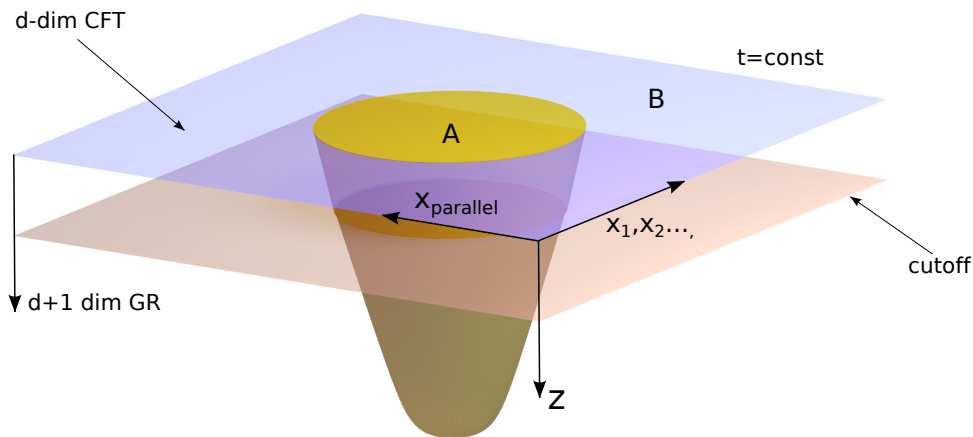


Figure 5: The extremal surface for the EE in the holographic calculation.

surface Σ_A with the same boundary as the subsystem A (see Figure 1) in the field theory, which is located on the AdS boundary. This has been proven by Lewkowycz and Maldacena [20]. The Ryu-Takayanagi formula (2.7) has been extended to time dependent systems [19], where the notion of a minimal surface is replaced by the one of an extremal surface. For more information regarding a mathematical proof for this case see [21].

From the AdC/CFT correspondence it follows that specific 2-dimensional CFTs are equivalent with gravitational theories on AdS_3 of radius L . The results for the EE using (2.7) agrees with (2.6). The central charge of the CFT is linked with the radius of AdS by

$$c = \frac{3L}{2G_N^3}. \quad (2.8)$$

It is interesting to note the similarity between equation (2.7) and the Bekenstein-Hawking entropy for black holes $S_{BH} = \frac{A_{BH}}{4G_N}$, where A_{BH} denotes the area of the black holes event horizon. There are many arguments for looking at this connection. An interesting question is if the S_{BH} can be understood as the EE [22].

For more and details see [3, 5].

2 BACKGROUND

2.6 Einstein equations

The Einstein equations are given by

$$R_{\mu\nu} - \frac{1}{2}Rg_{\mu\nu} + \Lambda g_{\mu\nu} = \frac{8\pi G}{c^4}T_{\mu\nu}, \quad (2.9)$$

where $R_{\mu\nu}$ is the Ricci curvature tensor, R is the Ricci scalar, $g_{\mu\nu}$ is the metric, Λ is the cosmological constant, G is the Newton constant, c is the speed of light and $T_{\mu\nu}$ is the stress-energy tensor. Defining the Einstein tensor

$$G_{\mu\nu} = R_{\mu\nu} - \frac{1}{2}Rg_{\mu\nu}, \quad (2.10)$$

the Einstein equations gain the following form

$$G_{\mu\nu} + \Lambda g_{\mu\nu} = \frac{8\pi G}{c^4}T_{\mu\nu}, \quad (2.11)$$

or written in geometrized units ($G = c = 1$)

$$G_{\mu\nu} + \Lambda g_{\mu\nu} = 8\pi T_{\mu\nu}. \quad (2.12)$$

AdS spacetime is the unique maximally symmetric solution of the Einstein equations in vacuum with constant negative curvature. Since we are interested in asymptotically AdS spacetime we use the line element in the Poincaré patch given by

$$(ds^2) = \frac{L^2}{r^2}dr^2 + \frac{r^2}{L^2}\eta_{\mu\nu}dx^\mu dx^\nu, \quad (2.13)$$

where L is the AdS radius and $\eta_{\mu\nu}$ is the $(d-1)$ -dimensional Minkowski metric. For the d -dimensional AdS spacetime the number of independent Riemann components (C_d), the Ricci scalar (R_d) and the cosmological constant (Λ_d) are given by

$$C_d = \frac{d^2(d^2-1)}{12}, \quad (2.14)$$

$$R_d = -\frac{d(d-1)}{L^2}, \quad (2.15)$$

$$\Lambda_d = -\frac{(d-1)(d-2)}{2L^2}. \quad (2.16)$$

Anisotropic asymptotically AdS_5 spacetime

Since we are interested in describing far from equilibrium plasmas, our focus is at the dynamics of the simplest homogeneous, anisotropic case, as proposed in [23, 24, 25, 9]. We are looking at the anisotropic line element given by

$$\begin{aligned} (ds)^2 &= g_{ab}dx^a \otimes dx^b + X^{2/3}(x^\alpha)g_{ij}(x^\alpha)dx^i \otimes dx^j \\ &= g_{ab}dx^a \otimes dx^b + X^{2/3}(x^\alpha)\left[e^{-2B(x^\alpha)}(dx^\parallel)^2 + e^{B(x^\alpha)}(dx^1)^2 + e^{B(x^\alpha)}(dx^2)^2\right], \end{aligned} \quad (2.17)$$

where $X(x^\alpha)$ and $B(x^\alpha)$ are real functions. The metric in (2.17)

$$g_{ij} = \begin{pmatrix} e^{-2B} & 0 & 0 \\ 0 & e^B & 0 \\ 0 & 0 & e^B \end{pmatrix}, \quad (2.18)$$

has unity determinant $\det[g_{ij}] = 1$. The function B encodes the anisotropy between x^\parallel and x^\perp .

Using the expressions introduced in equations (2.14)-(2.16) above, we obtain the Einstein equations in vacuum ($T_{\mu\nu} = 0$) for the AdS_5 with $L = 1$ (which provides $R = 20$ and $\Lambda = -6$)

$$R_{uv} + 4g_{uv} = 0. \quad (2.19)$$

3 Geometry

In this chapter we discuss the geometry that is used in the calculation of the entanglement entropy in an anisotropic system. First the $2d$ dilaton gravity is presented.

3.1 2-dimensional dilaton gravity

The 2-dimensional dilaton gravity is described by the following action [26]

$$S = \int d^2x \sqrt{-g} [\phi R + V(\phi)], \quad (3.1)$$

where ϕ is the dilaton field, R is the Ricci scalar in two dimensions and V represents a dilatonic potential.

Our motivation for considering the $2d$ dilaton gravity is that the 5-dimensional EH action (from the anisotropic line element (2.17)) can be scaled down to a 2-dimensional EH action (3.2) via a dimensional reduction [27]

$$S \propto \int d^2x \sqrt{-g} \left(RX - \frac{2}{3} \frac{(\nabla X)^2}{X} + \frac{3}{2} (\nabla B)^2 X - 2\Lambda X \right). \quad (3.2)$$

Furthermore, since the number of Riemann components in d dimensions is $\frac{d^2(d^2-1)}{12}$, for $d = 2$ this results only in the Ricci scalar. Therefore this is the lowest possible dimension with curvature. Also using spherical symmetry in Einstein gravity with $d \geq 4$ one can obtain generalised dilaton theories.

It is easily shown that the same $2d$ dilaton gravity action (3.2) arises from dimensional reduction of the EH action minimally coupled to a massless Klein-Gordon field, as shown in the following.

The action of the system is defined as

$$S = S_{EH} + S_{KG}, \quad (3.3)$$

where the EH bulk action and the Klein-Gordon action are given by

$$S_{EH} \propto \int d^5x \sqrt{-g^{(5)}} (R^{\mathcal{M}} - 2\Lambda), \quad (3.4)$$

$$S_{KG} \propto \int d^5x \sqrt{|g^{(5)}|} g^{\mu\nu} (\partial_\mu B) (\partial_\nu B). \quad (3.5)$$

$$(3.6)$$

Using the line-element (2.17) with $B = 0$ the Ricci scalar is

$$R^{\mathcal{M}} = R - \frac{2}{3} \frac{(\nabla X)^2}{X^2} - 6 \frac{\square X}{X}. \quad (3.7)$$

Setting all the results in the isotropic EH action and integrating over the 3 compact dimensions of the torus yields up to a boundary term

$$S \propto \int d^2x \sqrt{-g} \left(RX - \frac{2}{3} \frac{(\nabla X)^2}{X} + \frac{3}{2} (\nabla B)^2 X - 2\Lambda X \right), \quad (3.8)$$

where $(\nabla B)^2$ arises from the Klein-Gordon action.

As mentioned, the action above is equivalent to (3.2).

3.2 The map from anisotropic AdS_5 to isotropic AdS_5

As shown previously one can map the results of an anisotropic AdS_5 to isotropic $2d$ dilaton gravity system. We are considering the following line element in the isotropic case

$$(d\tilde{s})^2 = g_{ab}d\tilde{x}^a \otimes d\tilde{x}^b + X^{2/3}(\tilde{x}^\alpha) d\tilde{x}^i \otimes d\tilde{x}^j, \quad (3.9)$$

and for the anisotropic case the line element given in (2.17). We can rewrite these line elements in the Eddington-Finkelstein coordinates (see Appendix A) using $r = \frac{1}{z}$, which yields

$$(d\tilde{s})^2 = -Ad\tilde{t}^2 - \frac{2d\tilde{z}d\tilde{t}}{\tilde{z}^2} + \Sigma^2 d\tilde{x}^2, \quad (3.10)$$

$$(ds)^2 = -Adt^2 - \frac{2dzdt}{z^2} + \Sigma^2 \left[e^{-2B(z,t)} (dx^\parallel)^2 + e^{B(z,t)} (dx^1)^2 + e^{B(z,t)} (dx^2)^2 \right]. \quad (3.11)$$

At the boundary, $z \rightarrow 0$, the maps are trivial

$$(d\tilde{s})^2|_{z \rightarrow 0} = \frac{1}{\tilde{z}^2} \left(-d\tilde{t}^2 + d\tilde{x}^2 \right), \quad (3.12)$$

$$(ds)^2|_{z \rightarrow 0} = \frac{1}{z^2} \left(-dt^2 + d\bar{x}^2 \right). \quad (3.13)$$

Now considering finite value of $z \rightarrow \epsilon$ near the boundary, we obtain non-trivial maps

$$e^{-B(z=\epsilon,t)} dx^\parallel = d\tilde{x}^\parallel, \quad (3.14)$$

$$e^{B(z=\epsilon,t)/2} dx^1 = d\tilde{x}^1, \quad (3.15)$$

$$e^{B(z=\epsilon,t)/2} dx^2 = d\tilde{x}^2. \quad (3.16)$$

From the maps above one can obtain the coordinates in the anisotropic case

$$dx^\parallel = e^{B(z=\epsilon,t)} d\tilde{x}^\parallel, \quad (3.17)$$

$$dx^1 = e^{-B(z=\epsilon,t)/2} d\tilde{x}^1, \quad (3.18)$$

$$dx^2 = e^{-B(z=\epsilon,t)/2} d\tilde{x}^2. \quad (3.19)$$

3.3 Numerical approach to the Einstein equations

Solving the Einstein equations is a difficult task, since they form a set of non-linear partial differential equations. There are three leading methods that are used [28, 29]:

- the 3+1 formalism;
- the conformal formalism;
- the characteristic formalism.

3 GEOMETRY

The first two approaches split the spacetime into spacelike hypersurfaces[30] (in our case the 5-dimensional spacetime by 4-dimensional hypersurfaces). While in the 3+1 method the hypersurfaces reach spatial infinity and are restrained on an enclosed region, in the conformal method they are hyperboloidal reaching future null infinity. In the characteristic formulation lightlike hypersurfaces are used for the slicing. This decouples the Einstein equations into a nested set of ordinary differential equations (ODEs). Therefore it is more appropriate to study the development on the boundary of AdS/CFT using this method.

Einstein equations in the characteristic formulation

We use the original Eddington-Finkelstein coordinates with r instead of z yielding the line element

$$(ds)^2 = -Adt^2 + 2drdt + \Sigma^2 \left[e^{-2B(r,t)} (dx^\parallel)^2 + e^{B(r,t)} (dx^1)^2 + e^{B(r,t)} (dx^2)^2 \right]. \quad (3.20)$$

In the equation above now r represents the holographic coordinate ($r \rightarrow \infty$ corresponds to the boundary), t is the advanced time, x^\parallel , x^1 and x^2 are the spatial coordinates of the boundary and A , S and B are fields depending only on t and r . The Einstein equations in the characteristic formulation are now given by the simple form [23, 24, 25, 31, 32, 9]

$$0 = \Sigma \left(\dot{\Sigma} \right)' + 2\Sigma' \dot{\Sigma} - 2\Sigma^2, \quad (3.21)$$

$$0 = \Sigma \left(\dot{B} \right)' + \frac{3}{2} \left(\Sigma' \dot{B} + B' \dot{\Sigma} \right), \quad (3.22)$$

$$0 = A'' + 3B' \dot{\Sigma} - \frac{12\Sigma' \dot{\Sigma}}{\Sigma^2} + 4, \quad (3.23)$$

$$0 = \ddot{\Sigma} + \frac{1}{2} \left(\dot{B}^2 \Sigma - A' \dot{\Sigma} \right), \quad (3.24)$$

$$0 = \Sigma'' + \frac{1}{2} B'^2 \Sigma, \quad (3.25)$$

where the following notation for the derivatives along the ingoing and outgoing radial null geodesics for arbitrary functions $f(r, t)$ was used

$$f' = \partial_r f, \quad (3.26)$$

$$\dot{f} = \partial_t f + \frac{1}{2} A \partial_r f. \quad (3.27)$$

For solving the initial-value problem equations (3.21)-(3.25) are used. The benefit is that only linear ODEs in dependence of r at each time step need to be solved. The order of solving them is as follows: using B as initial condition, from equation (3.25) Σ can be found on the first time slice; now $\dot{\Sigma}$ can be obtained from (3.21); the next step is computing \dot{B} from (3.22); afterwards by integrating (3.23) A is obtained; lastly using (3.27) one calculates $\partial_t B$. From here on using Runge-Kutta algorithm one continues to the next time step.

Near-boundary expansion

Considering the asymptotically AdS_5 at $r \rightarrow \infty$, the metric functions can be expanded in a series

$$A(r, t) = \sum_{i=0}^4 a_i(t) r^{-i+2} + \mathcal{O}(r^{-3}), \quad (3.28)$$

$$B(r, t) = \sum_{i=0}^4 b_i(t) r^{-i} + \mathcal{O}(r^{-5}), \quad (3.29)$$

$$\Sigma(r, t) = \sum_{i=0}^4 \sigma_i(t) r^{-i+1} + \mathcal{O}(r^{-4}). \quad (3.30)$$

Inserting these expansions in equations (3.21)-(3.25) and using the derivatives (3.26) and (3.27) we obtain [9]

$$A(r, t) = (r + \xi(t))^2 - 2\partial_t \xi(t) + \frac{a_4}{r^2} - \frac{2a_4 \xi}{r^3} + \mathcal{O}(r^{-4}), \quad (3.31)$$

$$B(r, t) = \frac{b_4(t)}{r^4} + \frac{\partial_t b_4(t) - 4b_4(t)\xi(t)}{r^5} + \mathcal{O}(r^{-6}), \quad (3.32)$$

$$\Sigma(r, t) = r + \xi(t) - \frac{b_4^2}{7r^7} + \mathcal{O}(r^{-8}). \quad (3.33)$$

In the expressions above, at the first order of r the coefficient $\sigma_1(t)$ remains unknown and we used the gauge freedom by setting $\sigma_1(t) = \xi(t)$, where $\xi(t)$ is an arbitrary function. We can see that two coefficients, a_4 and $b_4(t)$, are undetermined and that a_4 is independent of t . This is due to the fact that the expansion was done up to the fourth order. Calculating higher orders in the expansion shows that the fifth order confines a_4 to be constant.

It is clear that the metric functions diverge near the boundary expansion. A neat way to regularize them with new functions is as follows

$$A_{reg}(z, t) = \frac{A(z, t) - \xi(t)^2 + 2\partial_t \xi(t)}{z^2} - 1 - 2\xi(t)z, \quad (3.34)$$

$$B_{reg}(z, t) = \frac{B(z, t)}{z^4}, \quad (3.35)$$

$$\Sigma_{reg}(z, t) = \frac{\Sigma(z, t) - \xi(t)}{z^4} - z^3, \quad (3.36)$$

$$\dot{B}_{reg}(z, t) = \frac{\dot{B}(z, t)}{z^3} \quad (3.37)$$

$$\dot{\Sigma}_{reg}(z, t) = \frac{\dot{\Sigma}(z, t)}{z^2} - \frac{\xi(t)^2}{2z^2} - \frac{\xi(t)}{z^3} - \frac{1}{2z^4}, \quad (3.38)$$

where we have reverted the substitution $r = \frac{1}{z}$.

Holographic stress-energy tensor

A precise expression for the stress-energy tensor, within the holographic renormalization correlated with the solutions of the Einstein equations for AdS , is presented

3 GEOMETRY

in [33]. This is achieved by rewriting the solutions in the Fefferman-Graham coordinates (FG) [34]

$$(ds)^2 = g_{\mu\nu} = \frac{l^2}{r^2} (dr^2 + g_{ij}(x, r) dx^i dx^j). \quad (3.39)$$

The stress-energy tensor reads ([33], see also [1, 9])

$$\langle T^{\mu\nu} \rangle = \frac{N_c^2}{2\pi^2} \text{diag} [\mathcal{E}, \mathcal{P}_{\parallel}(t), \mathcal{P}_1(t), \mathcal{P}_2(t)], \quad (3.40)$$

where \mathcal{E} represents the energy density and $\mathcal{P}_{\parallel}(t)$ and $\mathcal{P}_{1,2}(t)$ are the longitudinal and transversal pressure densities. The coefficients a_4 and $b_4(t)$ in the expansion above are related to the components of the stress energy tensor by the following relations

$$\mathcal{E} = -\frac{3}{4}a_4, \quad \mathcal{P}_{\parallel}(t) = -\frac{1}{4}a_4 - 2b_4(t), \quad \mathcal{P}_1(t) = \mathcal{P}_2(t) = -\frac{1}{4}a_4 + b_4(t). \quad (3.41)$$

Since a_4 is independent and $b_4(t)$ is dependent from t , one identifies the energy density to be constant and the pressure densities to be dependent of t . In Figure 6 the components of the stress-energy tensor given by (3.41) on the CFT side are shown. As one can see, while the energy density is constant, the transversal and longitudinal pressure thermalize after a few oscillations.

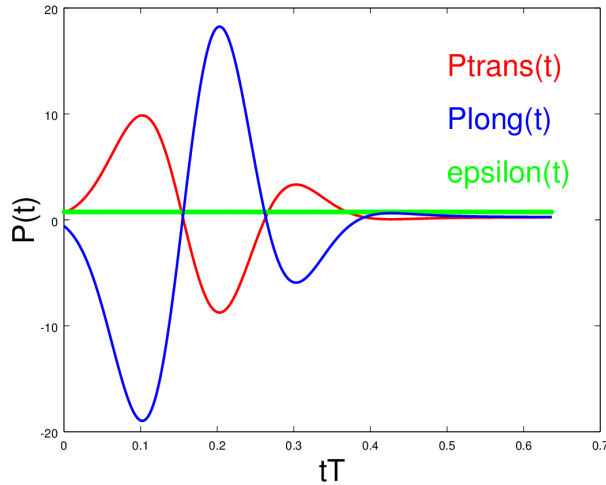


Figure 6: Energy density, transversal and longitudinal pressure.

4 The two point function and entanglement entropy for a spherical region

Our intention in this chapter is to present the computation of the 2PF for operators of large conformal weight and the HEE. Due to the non-local character of these observables, they provide a way to gain insight into the thermalization process of a system going beyond local observables, like the energy momentum tensor (EMT). Calculating the EE (which is relatively simple to compute in the holographic setup), in the boundary of CFT amounts to calculating an extremal surface in the bulk.

Calculating the EE as well as the 2PF reduces to finding geodesics, as shown in the following.

4.1 Two-point functions

It has been shown [35, 36], that the equal time of the 2PF for an operator \mathcal{O} of large conformal weight Δ can be expressed through a path integral

$$\langle \mathcal{O}(t, \vec{x}) \mathcal{O}(t, \vec{x}') \rangle = \int \mathcal{D}\mathcal{P} e^{-i\Delta\mathcal{L}(\mathcal{P})} \approx \sum_{\text{geodesics}} e^{-\Delta L_g} \approx e^{-\Delta L}. \quad (4.1)$$

Here the path integral is computed over all possible paths that connect the two points (t, \vec{x}) and (t, \vec{x}') , and $\mathcal{L}(\mathcal{P})$ denotes the length of the path. In the equation above the geodesic approximation does not take into account the perturbative corrections, where the integral over all paths is replaced by the sum of all geodesics. The second approximation is valid in the limit of large conformal weight of the operator and can be explained considering that at leading order only the geodesic with the smallest value of L_g contributes.

A problem that occurs is the divergence of the length of the geodesic due to the asymptotically AdS boundary. We choose to regularize by introducing a cutoff in the radial direction and subtracting the initial length of the geodesic's denoted by L_0

$$\langle \mathcal{O}(t, \vec{x}) \mathcal{O}(t, \vec{x}') \rangle_{ren} = e^{-L_{ren}}, \quad (4.2)$$

where

$$L_{ren} = \frac{L - L_0}{\Delta}. \quad (4.3)$$

In this way the geodesics end at a finite value near the infinite boundary.

Since we are using an anisotropic metric, in the calculation of the geodesics one can consider the endpoints to be separated in the longitudinal direction or in the transverse direction. In this thesis the longitudinal direction is chosen. Computing the geodesics requires that the geometry of the system is calculated at every point by solving the Einstein equations. By doing this the calculation is restricted to a certain coordinate range. It is worth noting here, that there exists only a definite number of geodesics that actually satisfy the initial conditions of the chosen region.

Finding (the length of) the geodesics is done by solving the geodesic equation of the corresponding line element of the $3d$ subspace, in this case the line element

$$(ds)^2 = -Adt^2 - \frac{2}{z^2} dzdt + \Sigma^2 (dx^\parallel)^2. \quad (4.4)$$

4.2 Holographic entanglement entropy for a spherical region from geodesics

We are considering the entanglement entropy on a spherical region. Our motivation for this are the symmetries that can be exploited in order to simplify the problem.

Let us consider the spherical region shown in Figure 7. Furthermore we are

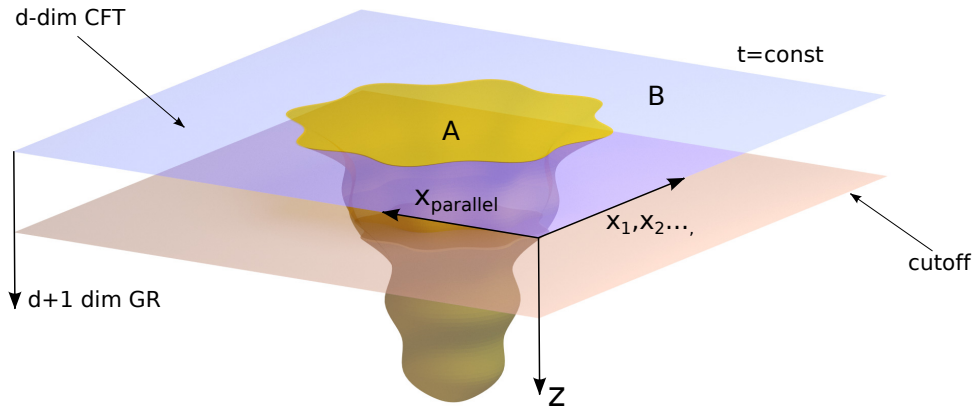


Figure 7: Spherical boundary region with minimal surface.

considering the boundary problem at the slice $t = const$.

As discussed in 2.1, the EE can be generalized to time dependent systems [19] with the equivalent boundary A by extremizing the surface functional

$$\mathcal{A} = \int d^3\sigma \sqrt{\det \left(\frac{\partial x^\mu}{\partial \sigma^a} \frac{\partial x^\nu}{\partial \sigma^b} g_{\mu\nu} \right)}. \quad (4.5)$$

Applying the spherical symmetries in the spatial dimensions (since we examine a spherical region), we arrive to calculating the extremal area functional by finding the geodesics. This is shown by parametrising the line element of a spherical region (see Appendix B).

Now we introduce an auxiliary spacetime. The line element can be written as

$$(ds)^2 = \eta_{ab} dx^a \otimes dx^b + \Phi_\parallel^2 (dx^\parallel)^2 + \Phi_1^2 (dx^1)^2 + \Phi_2^2 (dx^2)^2 \quad (4.6)$$

$$= h_{\alpha\beta} dx^\alpha \otimes dx^\beta + \Phi_1^2 (dx^1)^2 + \Phi_2^2 (dx^2)^2, \quad (4.7)$$

4 THE TWO POINT FUNCTION AND ENTANGLEMENT ENTROPY FOR A SPHERICAL REGION

where $h_{\alpha\beta}$ is the induced metric in dependency of (z, t, x^\parallel) . The surface functional with the induced metric is now

$$\mathcal{A} = \int \int \int dx^1 dx^2 d\sigma \sqrt{\Phi_1^2 \Phi_2^2 h_{\alpha\beta} \frac{\partial x^\alpha}{d\sigma} \frac{\partial x^\beta}{d\sigma}}. \quad (4.8)$$

The observed region has finite size, and from the first two integrals above we obtain only a constant (volume) factor, by which we divide in order to acquire normalized results. With this the calculation is abbreviated from $5 - d$ to $3 - d$. Inserting the expressions for $\Phi_1 = \Phi_2 = \Sigma$ we obtain the auxiliary spacetime line element

$$\begin{aligned} (ds)^2 &= h_{\alpha\beta} dx^\alpha dx^\beta \\ &= \Sigma^4 \left(-Adt^2 - \frac{2}{z^2} dzdt + \Sigma^2 (dx^\parallel)^2 \right). \end{aligned} \quad (4.9)$$

4.3 Calculating the geodesic

Since the computation of the extremal surfaces reduces to calculating the curves of extremal length (see above), the geodesic equation is parametrised by an affine parameter and it needs to be solved

$$\ddot{x}^\mu + \Gamma_{\nu\lambda}^\mu \dot{x}^\nu \dot{x}^\lambda = 0, \quad (4.10)$$

where the dot above refers to the derivative with respect to the affine parameter. It is beneficial to use a non-affine parameter for the numerical computation, $\tau(\sigma)$, which transforms equation (4.10) to

$$\ddot{x}^\mu + \Gamma_{\nu\lambda}^\mu \dot{x}^\nu \dot{x}^\lambda = -Jx^\mu. \quad (4.11)$$

Here the dot denotes the derivative with respect to the non-affine parameter and J is the Jacobian emerging from the change of parametrization.

In order to solve the partial differential equations numerically a relaxation scheme is used. This method for solving differential equations with boundary constraints is suitable for our interest, since we are looking at asymptotically AdS spacetime. It is an iterative process, which needs an ansatz that is improved to a certain point until we are satisfied with the order of uncertainty.

5 Numerical results

In the interest of obtaining numerical results for the 2PF and the EE, we gain the geometry from an Octave code (as done in [1]) and then calculate the observables with a Mathematica package introduced in [2] using a relaxation method.

Considering an isotropic case we set the scalar field $B = 0$ in (2.17) while calculating the geodesics. With these results the 2PF and the EE of a spherical region are calculated. We mapped these results to a spherical region in an anisotropic system as described in subsection 3.2. It is important to notice here, that while the calculated geodesics represent extremal surfaces in the isotropic case, after the mapping they are no longer extremal surfaces in the anisotropic case.

Different simulations are done in dependence of the spatial separation l_0 of the considered points at the boundary, where for the EE the values are smaller compared to the ones for the 2PF. The time evolution is chosen to be $t \in [0, 2]$. Here t and l_0 are arbitrary units for length and time, and the unit for the holographic coordinate is measured in units of the AdS radius.

The time evolution is performed with iteration, where the result from the previous step is taken as ansatz for the next time step.

Since the scalar B -field that generates the anisotropy is used in the following sections, it is displayed in Figure (8).

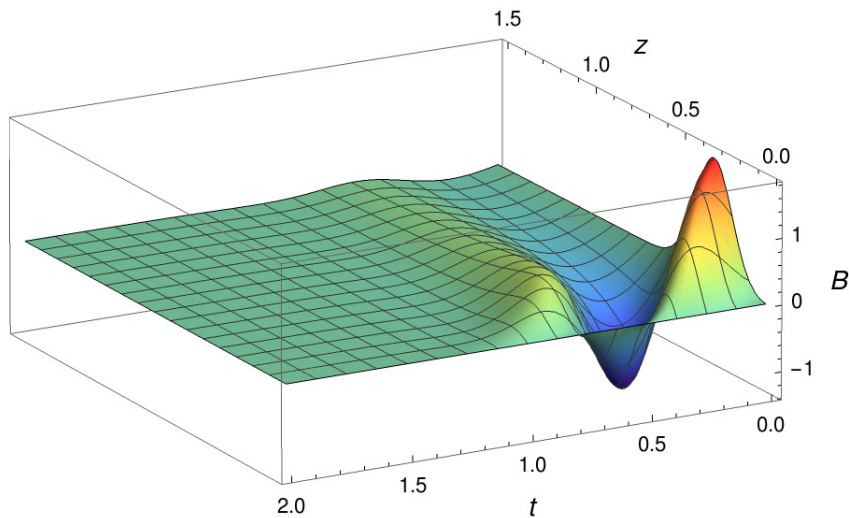


Figure 8: B -field.

For more information regarding the details for the numerical calculation see [1, 2].

5.1 Time evolution of the two-point function

We start with the numerical results for the two-point function. They are shown in Figure 9 for different separations, where the initial value was subtracted in order to gain more suitable results, as explained in subsection (4.1). As we can see the correlations start at an initial time and then thermalize to a constant value after a certain time. The difference between the final values after the thermalization is larger for larger separations.

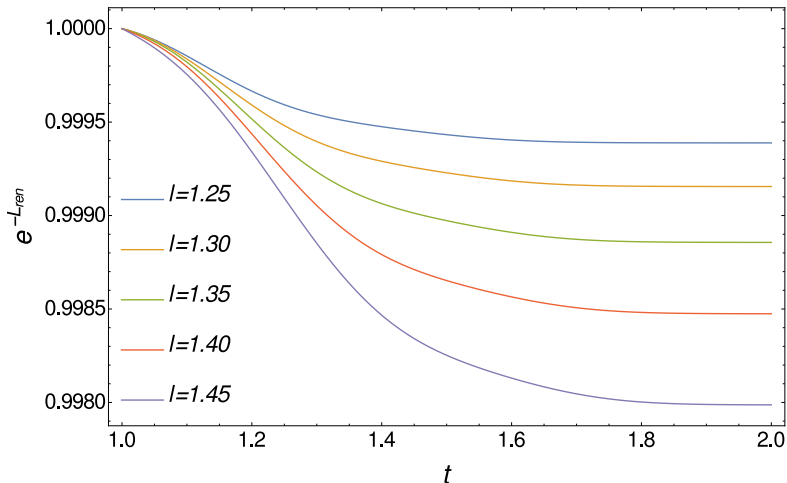


Figure 9: Time evolution of the two-point function for different separations.

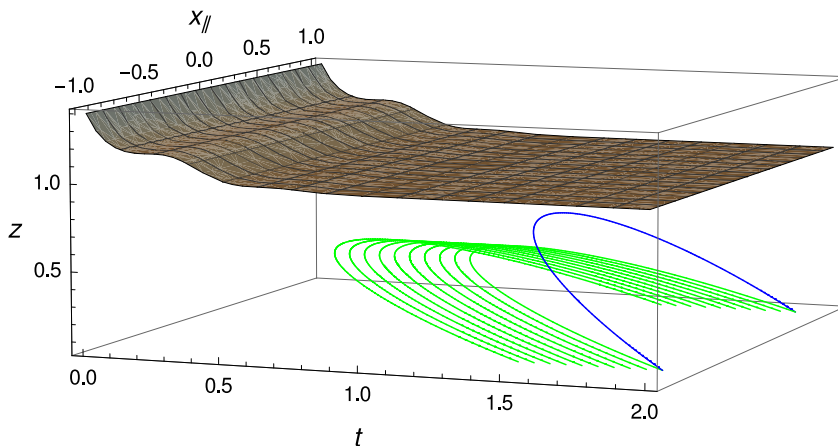


Figure 10: Time evolution of the geodesics for the two-point function (green) in the isotropic case with the ansatz (blue) and the apparent horizon (brown surface).

In Figure 10 the geodesics after the time evolution (green curves) are shown together with the ansatz (blue curve) and the apparent horizon. The radial position of the apparent horizon is represented by the brown surface. After the mapping of the parallel and transversal coordinates to the anisotropic case we obtain the geodesics shown in Figure 11 and 12. The green curves are the geodesics before the mapping and the red curves display the geodesics after the mapping in the

5 NUMERICAL RESULTS

anisotropic case. One can see that after the mapping each geodesic at a earlier time has bigger deformation than before. These deformations differ for the parallel and transverse direction. Although these geodesics are not the extremal surfaces in the anisotropic case, this shows a good way to establish a connection between the anisotropic and isotropic case. The main motivation of this is the easier computation.

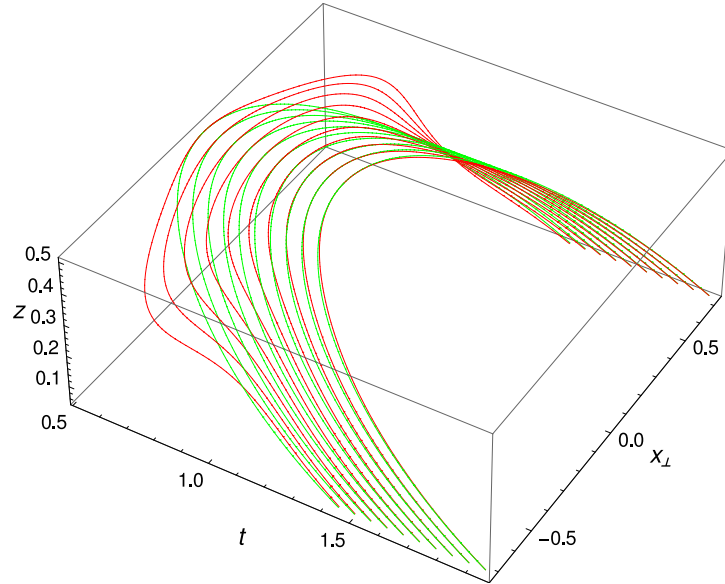


Figure 11: Geodesics after mapping the parallel coordinate for the anisotropic case (red curves) compared with the ones in the isotropic case calculated for the two-point function.

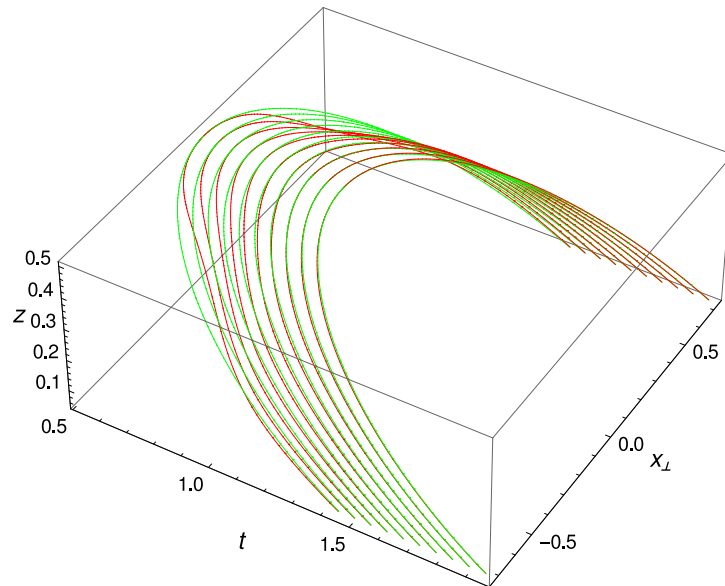


Figure 12: Geodesics after mapping the transversal coordinate for the anisotropic case (red curves) compared with the ones in the isotropic case calculated for the two-point function.

5.2 Time evolution of the entanglement entropy

In this section we observe the numerical results for the EE. Similar as for the 2PF, first the EE in dependence of different separations is shown in Figure 13. For the EE smaller values for the separation are used with wider range compared to the 2PF. Similar to the 2PF, the EE entropy thermalizes after a certain time to a constant value, which is below the initial one. For larger separations the final values are even lower. Also the difference between the thermal values grows with the separation. The main difference compared to the 2PF is that the EE at early times grows before it falls to the final value.

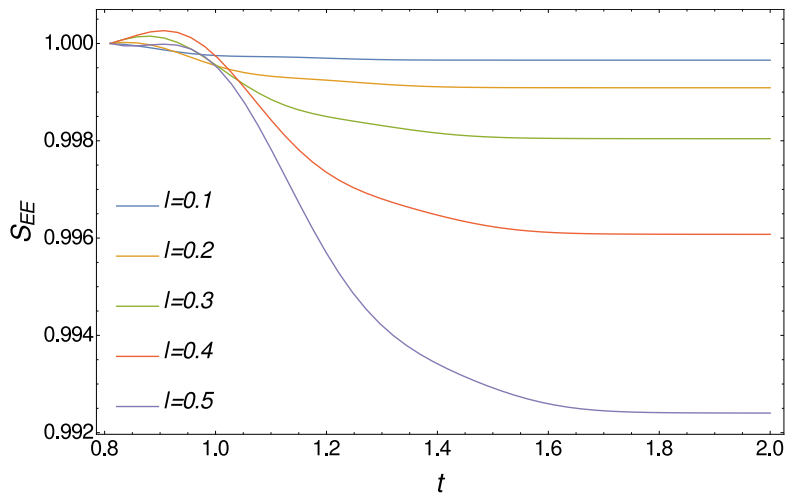


Figure 13: Time evolution of the entanglement entropy for different separations.

The time evolution of the geodesics for the EE (green curves) in the isotropic case differs from the one for the two-point function, as one can see in Figure 14. Again the ansatz is shown in blue, the apparent horizon is the brown surface and the energy density is shown in the contour plot.

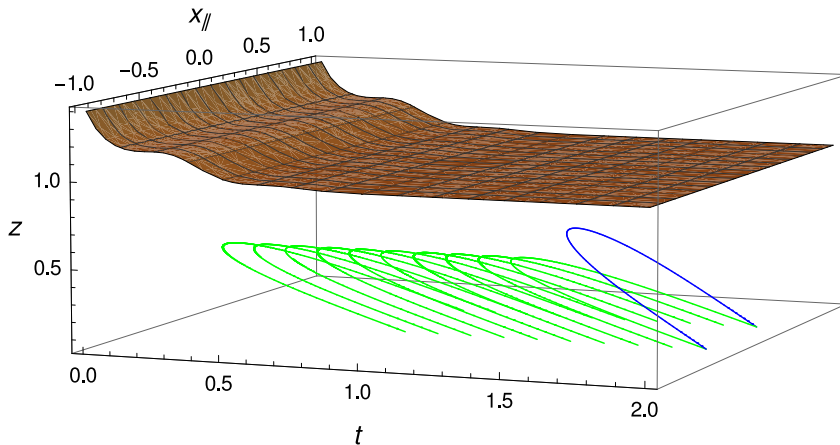


Figure 14: Time evolution of the geodesics for the entanglement entropy in the isotropic case with the ansatz, the apparent horizon and the energy density.

5 NUMERICAL RESULTS

After performing the mapping to the anisotropic case we obtain the geodesics shown in Figure 15 and 16. It is clear that the geodesics for the EE in the anisotropic case are more deformed as for the 2PF.

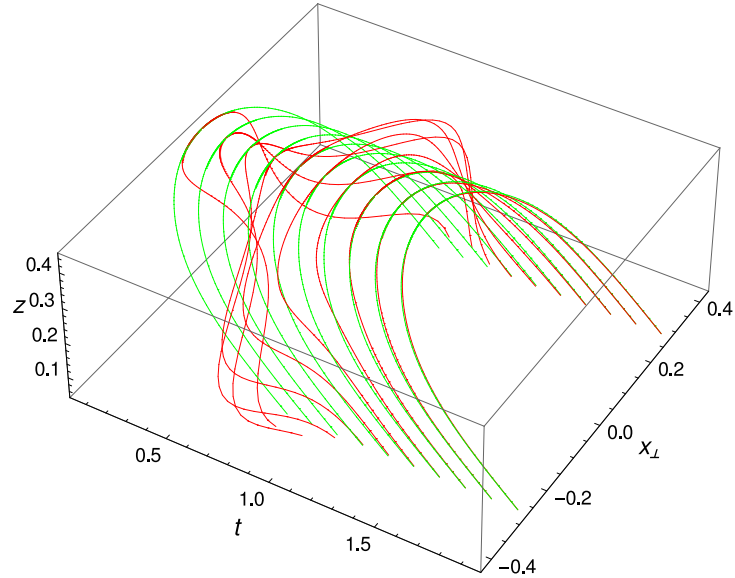


Figure 15: Geodesics after mapping the parallel coordinate for the anisotropic case (red curves) compared with the ones in the isotropic case calculated for the entanglement entropy.

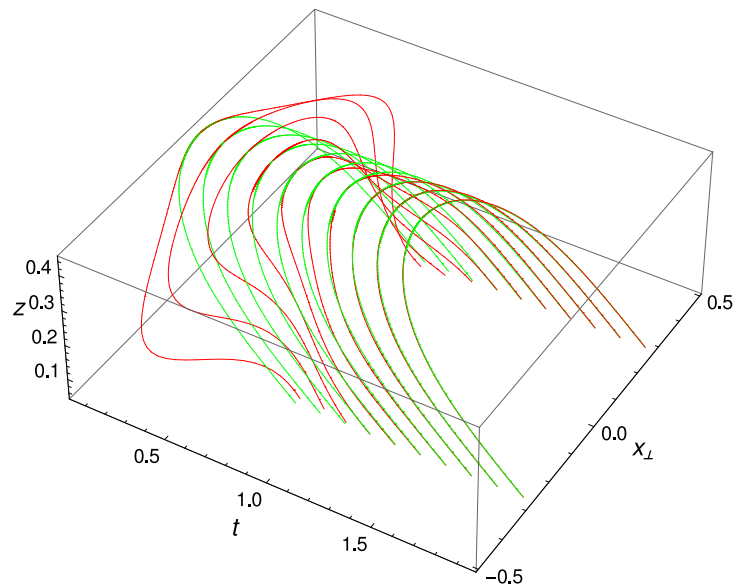


Figure 16: Geodesics after mapping and transversal coordinate for the anisotropic case (red curves) compared with the ones in the isotropic case calculated for the entanglement entropy.

6 Conclusion and outlook

6.1 Conclusion

In this work the holographic principle was used in order to calculate the two-point function for operators of large conformal weight and the entanglement entropy. We used a special case of this principle, namely the Anti de-Sitter/conformal field theory correspondence. The motivation for this is the fact, that this duality provides the opportunity to look at problems, that were not accessible otherwise.

The main application regards heavy ion collisions in high energy physics. In such collisions a new state of matter is formed, the quark-gluon plasma. $\mathcal{N} = 4$ supersymmetric Yang-Mills theory was considered as a model for describing the quark-gluon plasma, due to the similarities of this theory with quantum chromodynamics, that arise at high energies.

The calculation of the two-point function reduces to the computation of geodesics and the entanglement entropy to extremal co-dimension 2-surfaces. The main topic of this thesis was to calculate these observables in an isotropic system and then translate them into an anisotropic one. The interest for doing this is presented in [27]. It is shown that a specific anisotropic action is equivalent to an isotropic one plus a scalar field. These two actions are equivalent to a certain 2-dimensional dilaton gravity model with a massless non-minimally coupled scalar field. In an isotropic spacetime, considering simple regions like spheres, the extremal surfaces essentially reduce to the geodesics length times a constant volume factor.

First the Einstein equations were solved in the characteristic formulation using an Octave code, which implements the near-boundary expansion. Thereby the needed metric is calculated. The numerical computation of the observables was done in a Mathematica package, providing the time evolution of the quantities we want to examine.

The two-point function was calculated for different separations. The correlations were computed at the same initial time, but after the performed time evolution they thermalized to distinct constant values. These differed even more for larger separations. Next the geodesics were mapped to the anisotropic case for the transversal and parallel direction in order to see the differences from the isotropic case. At earlier times the geodesics in the anisotropic case have bigger deviations from the geodesics in the isotropic case. However, after the time-evolution they coincide.

The same numerical process was performed for the entanglement entropy. Although the entanglement entropy also thermalizes to constant values, the results differ from the ones obtained for the two-point function. Here smaller values in a larger range were taken into account, and for larger separation lengths the thermal values differ more. One essential distinction from the two-point function is that the entanglement entropy at the beginning of the time evolution first starts to grow and then thermalizes to a constant value below the initial one. Also after the mapping to the anisotropic case the geodesics in the transversal and parallel direction are more deformed.

The numerical calculations for these observables were done by considering a spherical boundary region. For different boundary regions, particularly for infinite stripe regions, the results have been shown in [1]. From here one can conclude that

the chosen boundaries have a great effect on the end results.

The initial conditions have played a large role in the computations. Since the observables vary very little in dependence of the separations, many calculations were done in order to obtain a better view of the development during the time evolution of the two-point function and the entanglement entropy.

6.2 Outlook

A number of challenges and questions still remains open. We have considered a compact region. Due to the fact that finding the extremal surfaces in an anisotropic system for this case is a demanding task, we were encouraged by the dimensional reduction to calculate geodesics in an isotropic system and then map them to the anisotropic system. Although this looked like a promising concept, the extremal surfaces computed in the isotropic case are no longer extremal surfaces in the anisotropic one. It is a challenging task to find the exact mapping. Still there are other ways to compute these surfaces. One tool is the Surface Evolver [37], where the area of a surface is minimized. But even here the question is, if the calculated minimal surface is the real minimal surface of the chosen region. Furthermore, in the Mathematica package that was used, the two-point function was calculated in the geodesic approximation. This can be improved by computing the exact two-point function, where a scalar field is added in the gravitational theory. Another interesting point that lies ahead is to look at compact regions in other geometries.

A Eddington-Finkelstein coordinates

We perform now a coordinate transformation in the Eddington-Finkelstein coordinates in order to obtain a metric of the following form

$$\begin{pmatrix} 0 & f_3(t, z) & 0 & 0 & 0 \\ f_1(t, z) & f_2(t, z) & 0 & 0 & 0 \\ 0 & 0 & \Sigma^2(t, z) & 0 & 0 \\ 0 & 0 & 0 & \Sigma^2(t, z) & 0 \\ 0 & 0 & 0 & 0 & \Sigma^2(t, z) \end{pmatrix}. \quad (\text{A.1})$$

Our line element is

$$\begin{aligned} (ds)^2 &= g_{tt}dt^2 + g_{zz}dz^2 + X^{2/3} \left[(dx^\parallel)^2 + (dx^1)^2 + (dx^2)^2 \right] \\ &= -g_{tt}dt^2 + g_{zz}dz^2 + \Sigma^2 d\vec{x}^2, \end{aligned}$$

where in the second line was used $g_{tt} \rightarrow -g_{tt}$, since the metric is $(-1, 1, 1, 1, 1)$ and $\Sigma^2 = X^{2/3}$. The transformation to the generalized Eddington-Finkelstein coordinates is

$$v = t + \int \sqrt{\frac{g_{zz}}{g_{tt}}} dz, \quad (\text{A.2})$$

from where it follows

$$dv = dt + \sqrt{\frac{g_{zz}}{g_{tt}}} dz. \quad (\text{A.3})$$

Setting this in the line element we obtain

$$\begin{aligned} (ds)^2 &= -g_{tt} \left(dv - \sqrt{\frac{g_{zz}}{g_{tt}}} dz \right)^2 + g_{zz} dz^2 + X^{2/3} \left[(dx^\parallel)^2 + (dx^1)^2 + (dx^2)^2 \right] \\ &= -g_{tt} dv^2 + 2\sqrt{g_{tt}g_{zz}} dv dz + \Sigma^2 d\vec{x}^2. \end{aligned} \quad (\text{A.4})$$

The metric is now given by

$$\tilde{g}_{uv} = \begin{pmatrix} -g_{tt} & \sqrt{g_{tt}g_{zz}} & 0 & 0 & 0 \\ \sqrt{g_{tt}g_{zz}} & 0 & 0 & 0 & 0 \\ 0 & 0 & \Sigma^2 & 0 & 0 \\ 0 & 0 & 0 & \Sigma^2 & 0 \\ 0 & 0 & 0 & 0 & \Sigma^2 \end{pmatrix}. \quad (\text{A.5})$$

From here one can choose different notations for the entries in the metric above.

B Parametrising the spherical region

Here the parametrization using the symmetries of an isotropic system is explicitly shown. Additionally we use two approaches to calculate the Christoffel symbols in order to see if they match, thereby confirming the validity of the parametrization:

on the one hand from the action and on the other one from their definition in terms of the metric function.

Writing the isotropic line element (3.9)

$$\begin{aligned} (ds)^2 &= g_{ab} dx^a \otimes dx^b + X^{2/3} \left[(dx^\parallel)^2 + (dx^1)^2 + (dx^2)^2 \right] \\ &= g_{tt} dt^2 + g_{zz} dz^2 + X^{2/3} \left[(dx^\parallel)^2 + (dx^1)^2 + (dx^2)^2 \right], \end{aligned} \quad (\text{B.1})$$

in spherical coordinates one yields

$$(ds)^2 = g_{tt} dt^2 + g_{zz} dz^2 + X^{2/3} \left[d\rho^2 + \rho^2 d\theta^2 + \rho^2 \sin^2(\theta) d\varphi^2 \right]. \quad (\text{B.2})$$

The line element can be rewritten as

$$\begin{aligned} (ds)^2 &= g_{tt} dt^2 + g_{zz} dz^2 + X^{2/3} \rho^2 \left[\frac{d\rho^2}{\rho^2} + d\theta^2 + \sin^2(\theta) d\varphi^2 \right] \\ &= g_{tt} dt^2 + g_{zz} dz^2 + \Omega^2 \left[dR^2 + d\theta^2 + \sin^2(\theta) d\varphi^2 \right], \end{aligned} \quad (\text{B.3})$$

where $\Omega^2 = X^{2/3} \rho^2$ and $dR^2 = d\rho^2/\rho^2$, and it follows $R = \ln(\rho)$. As it can be seen from the equation above the metric transforms to

$$g_{uv} = \begin{pmatrix} g_{tt} & 0 & 0 & 0 & 0 \\ 0 & g_{zz} & 0 & 0 & 0 \\ 0 & 0 & \Omega^2 & 0 & 0 \\ 0 & 0 & 0 & \Omega^2 & 0 \\ 0 & 0 & 0 & 0 & \Omega^2 \sin^2(\varphi) \end{pmatrix}. \quad (\text{B.4})$$

By parametrization with the parameter τ

$$h_{ij} d\sigma^i \otimes d\sigma^j = f^2(\tau) \left(d\tau^2 + d\tilde{\theta}^2 + \sin^2(\tilde{\theta}) d\tilde{\varphi}^2 \right), \quad (\text{B.5})$$

the induced metric h_{ij} is given by

$$h_{ij} = \begin{pmatrix} f^2(\tau) & 0 & 0 \\ 0 & f^2(\tau) & 0 \\ 0 & 0 & f^2(\tau) \sin^2(\tilde{\theta}) \end{pmatrix}. \quad (\text{B.6})$$

Due to the rotation symmetry $R = R(\tau)$, $z = z(\tau)$, while θ and φ do not depend on τ . Starting from the definition of the induced metric

$$h_{ij} = \frac{\partial x^u}{\partial \sigma^i} \frac{\partial x^v}{\partial \sigma^j} g_{uv}, \quad (\text{B.7})$$

the element $h_{\tau\tau}$ can be calculated

$$h_{\tau\tau} = \frac{\partial x^u}{\partial \tau} \frac{\partial x^v}{\partial \tau} g_{uv} = \frac{\partial t}{\partial \tau} \frac{\partial t}{\partial \tau} g_{tt} + \frac{\partial z}{\partial \tau} \frac{\partial z}{\partial \tau} g_{zz} + \frac{\partial R}{\partial \tau} \frac{\partial R}{\partial \tau} \Omega^2 = \dot{t}^2 g_{tt} + \dot{z}^2 g_{zz} + \dot{R}^2 \Omega^2. \quad (\text{B.8})$$

From equation (B.6) it follows

$$f(\tau) = \sqrt{\dot{t}^2 g_{tt} + \dot{z}^2 g_{zz} + \dot{R}^2 \Omega^2}. \quad (\text{B.9})$$

B PARAMETRISING THE SPHERICAL REGION

Setting the substitution done above yields

$$f(\tau) = \sqrt{\dot{t}^2 g_{tt} + \dot{z}^2 g_{zz} + \left(\frac{\partial}{\partial \tau} \ln(\rho)\right) X^{2/3} \rho^2} = \sqrt{\dot{t}^2 g_{tt} + \dot{z}^2 g_{zz} + X^{2/3} \dot{\rho}^2}. \quad (\text{B.10})$$

Now starting with the Nambu-Goto action

$$S_{NG} \propto \int d^n \sigma \sqrt{-|h|}, \quad (\text{B.11})$$

where h is the induced metric, we obtain

$$S_{NG} \propto \int d^3 \sigma \sqrt{f^6(\tau) \sin^2(\tilde{\theta})} = \int d\tau d\tilde{\theta} d\tilde{\varphi} f^3(\tau) \sin(\tilde{\theta}) = 4\pi \int d\tau f^3(\tau). \quad (\text{B.12})$$

The integral above calculates the length of a curve.

In order to show that this is indeed the length of the geodesic, we calculate the corresponding Christoffel symbols using two different approaches:

- Setting the result for $f(\tau)$ in the Nambu-Goto action we obtain

$$S_{NG} \propto 4\pi \int d\tau (\dot{t}^2 g_{tt} + \dot{z}^2 g_{zz} + X^{2/3} \dot{\rho}^2)^{3/2}. \quad (\text{B.13})$$

Performing the variation of the Nambu-Goto action and setting it zero yields

$$\delta S_{NG} \propto \frac{3}{2} 4\pi \int d\tau f(\tau) \left[2\dot{t}\delta\dot{t}g_{tt} + \dot{t}^2 \frac{\partial g_{tt}}{\partial t} \delta t + 2\dot{z}\delta\dot{z}g_{zz} + \dot{z}^2 \frac{\partial g_{zz}}{\partial z} \delta z + \right. \\ \left. \dot{\rho}^2 \frac{2}{3} X^{-1/3} \left(\frac{\partial X}{\partial t} \delta t + \frac{\partial X}{\partial z} \delta z \right) + 2\dot{\rho}\delta\dot{\rho}X^{2/3} \right] \quad (\text{B.14})$$

$$\stackrel{!}{=} 0. \quad (\text{B.15})$$

Now the Euler-Lagrange equations

$$\frac{\partial L}{\partial q_i} - \frac{\partial}{\partial \tau} \frac{\partial L}{\partial \dot{q}_i} = 0, \quad (\text{B.16})$$

for each coordinate can be calculated

$$-\partial_\tau (2f\dot{t}g_{tt}) + f\dot{t}^2 \frac{\partial g_{tt}}{\partial t} + f\dot{\rho}^2 \frac{2}{3} X^{-1/3} \frac{\partial X}{\partial t} = 0, \quad (\text{B.17})$$

$$-\partial_\tau (2f\dot{z}g_{zz}) + f\dot{z}^2 \frac{\partial g_{zz}}{\partial z} + f\dot{\rho}^2 \frac{2}{3} X^{-1/3} \frac{\partial X}{\partial z} = 0, \quad (\text{B.18})$$

$$-\partial_\tau (2f\dot{\rho}X^{2/3}) = 0. \quad (\text{B.19})$$

The first equation can be rewritten as

$$-2\dot{f}\dot{t}g_{tt} - 2f\ddot{t}g_{tt} - 2f\dot{t}\dot{g}_{tt} + f\dot{t}^2 \frac{\partial g_{tt}}{\partial t} + f\dot{\rho}^2 \frac{2}{3} X^{-1/3} \frac{\partial X}{\partial t} = 0. \quad (\text{B.20})$$

Now the equation for t becomes

$$\frac{\dot{f}}{f} \dot{t} + \ddot{t} + \frac{\dot{g}_{tt}}{g_{tt}} \dot{t} - \frac{1}{2} \frac{\partial g_{tt}}{\partial t} \frac{1}{g_{tt}} \dot{t} - \frac{1}{3} X^{-1/3} \frac{\partial X}{\partial t} \frac{1}{g_{tt}} \dot{\rho}^2 = 0, \quad (\text{B.21})$$

or rewritten as

$$\ddot{t} - \frac{1}{2} \frac{\partial g_{tt}}{\partial t} \frac{1}{g_{tt}} \dot{t}^2 - \frac{1}{3} \frac{\partial X}{\partial t} \frac{1}{g_{tt}} X^{-1/3} \dot{\rho}^2 = - \left(\frac{\dot{f}}{f} + \frac{\dot{g}_{tt}}{g_{tt}} \right) \dot{t}.$$

Here \dot{g}_{tt} is given by

$$\begin{aligned} \dot{g}_{tt} &= \frac{\partial g_{tt}}{\partial t} \frac{\partial t}{\partial \tau} + \frac{\partial g_{tt}}{\partial z} \frac{\partial z}{\partial \tau} + \frac{\partial g_{tt}}{\partial \rho} \frac{\partial \rho}{\partial \tau} \\ &= \frac{\partial g_{tt}}{\partial t} \dot{t} + \frac{\partial g_{tt}}{\partial z} \dot{z} + \frac{\partial g_{tt}}{\partial \rho} \dot{\rho}. \end{aligned} \quad (\text{B.22})$$

Setting this result we obtain

$$\ddot{t} - \frac{1}{2} \frac{\partial g_{tt}}{\partial t} \frac{1}{g_{tt}} \dot{t}^2 - \frac{1}{3} \frac{\partial X}{\partial t} \frac{1}{g_{tt}} X^{-1/3} \dot{\rho}^2 + \frac{1}{g_{tt}} \left(\frac{\partial g_{tt}}{\partial t} \dot{t} + \frac{\partial g_{tt}}{\partial z} \dot{z} + \frac{\partial g_{tt}}{\partial \rho} \dot{\rho} \right) \dot{t} = - \frac{\dot{f}}{f} \dot{t}. \quad (\text{B.23})$$

Rearranging the terms results with

$$\ddot{t} + \frac{1}{2} \frac{\partial g_{tt}}{\partial t} \frac{1}{g_{tt}} \dot{t}^2 - \frac{1}{3} \frac{\partial X}{\partial t} \frac{1}{g_{tt}} X^{-1/3} \dot{\rho}^2 + \frac{1}{g_{tt}} \frac{\partial g_{tt}}{\partial z} \dot{t} \dot{z} + \frac{1}{g_{tt}} \frac{\partial g_{tt}}{\partial \rho} \dot{t} \dot{\rho} = - \frac{\dot{f}}{f} \dot{t}. \quad (\text{B.24})$$

Analog for the z coordinate we gain

$$\ddot{z} + \frac{1}{2} \frac{\partial g_{zz}}{\partial z} \frac{1}{g_{zz}} \dot{z}^2 - \frac{1}{3} \frac{\partial X}{\partial z} \frac{1}{g_{zz}} X^{-1/3} \dot{\rho}^2 + \frac{1}{g_{zz}} \frac{\partial g_{zz}}{\partial t} \dot{z} \dot{t} + \frac{1}{g_{zz}} \frac{\partial g_{zz}}{\partial \rho} \dot{z} \dot{\rho} = - \frac{\dot{f}}{f} \dot{z}. \quad (\text{B.25})$$

Finally the equation for the ρ coordinate is computed

$$\dot{f} \dot{\rho} X^{2/3} + f \ddot{\rho} X^{2/3} + \frac{2}{3} f \dot{\rho} X^{-1/3} \left(\frac{\partial X}{\partial t} \dot{t} + \frac{\partial X}{\partial z} \dot{z} \right) = 0, \quad (\text{B.26})$$

which can be rewritten as

$$\ddot{\rho} + \frac{2}{3} \frac{1}{X} \left(\frac{\partial X}{\partial t} \dot{t} + \frac{\partial X}{\partial z} \dot{z} \right) \dot{\rho} = - \frac{\dot{f}}{f} \dot{\rho}. \quad (\text{B.27})$$

From the geodesic equation

$$\ddot{x}^\mu + \Gamma_{\nu\lambda}^\mu \dot{x}^\nu \dot{x}^\lambda = 0, \quad (\text{B.28})$$

some of the Christoffel symbols can be identified straightaway from equations (B.24) and (B.25)

$$\Gamma_{tt}^t = \frac{1}{2} \frac{\partial g_{tt}}{\partial t} \frac{1}{g_{tt}}, \quad \Gamma_{\rho\rho}^t = - \frac{1}{3} \frac{\partial X}{\partial t} \frac{1}{g_{tt}} X^{-1/3}, \quad (\text{B.29})$$

$$\Gamma_{zz}^z = \frac{1}{2} \frac{\partial g_{zz}}{\partial z} \frac{1}{g_{zz}}, \quad \Gamma_{\rho\rho}^z = - \frac{1}{3} \frac{\partial X}{\partial z} \frac{1}{g_{zz}} X^{-1/3}. \quad (\text{B.30})$$

B PARAMETRISING THE SPHERICAL REGION

For the two last Christoffel symbols from equations (B.24) and (B.25) the symmetry $\Gamma_{jk}^i = \Gamma_{kj}^i$ must be considered. This gives

$$\Gamma_{tz}^t + \Gamma_{zt}^t = \frac{1}{g_{tt}} \frac{\partial g_{tt}}{\partial z}, \quad \Gamma_{t\rho}^t + \Gamma_{\rho t}^t = \frac{1}{g_{tt}} \frac{\partial g_{tt}}{\partial \rho}, \quad (\text{B.31})$$

which results with

$$\Gamma_{tz}^t = \Gamma_{zt}^t = \frac{1}{2} \frac{1}{g_{tt}} \frac{\partial g_{tt}}{\partial z}, \quad \Gamma_{t\rho}^t = \Gamma_{\rho t}^t = \frac{1}{2} \frac{1}{g_{tt}} \frac{\partial g_{tt}}{\partial \rho}. \quad (\text{B.32})$$

The same is for the z coordinate

$$\Gamma_{zt}^z = \Gamma_{tz}^z = \frac{1}{2} \frac{1}{g_{zz}} \frac{\partial g_{zz}}{\partial t}, \quad \Gamma_{z\rho}^z = \Gamma_{\rho z}^z = \frac{1}{2} \frac{1}{g_{zz}} \frac{\partial g_{zz}}{\partial \rho}. \quad (\text{B.33})$$

From equation (B.27) the following Christoffel symbols can be obtained (again having in mind the symmetry of the Christoffel symbols)

$$\Gamma_{\rho t}^\rho = \Gamma_{t\rho}^\rho = \frac{1}{2} \frac{2}{3} \frac{1}{X} \frac{\partial X}{\partial t} = \frac{1}{3} \frac{1}{X} \frac{\partial X}{\partial t}, \quad \Gamma_{\rho z}^\rho = \Gamma_{z\rho}^\rho = \frac{1}{2} \frac{2}{3} \frac{1}{X} \frac{\partial X}{\partial z} = \frac{1}{3} \frac{1}{X} \frac{\partial X}{\partial z}. \quad (\text{B.34})$$

The last equation can also be written as

$$\Gamma_{\rho t}^\rho = \frac{1}{3} \frac{\partial}{\partial z} \ln(X), \quad \Gamma_{\rho z}^\rho = \frac{1}{3} \frac{\partial}{\partial t} \ln(X). \quad (\text{B.35})$$

- Now we start with the second approach. On the other hand it holds

$$h = (\dot{x}^\mu \dot{x}^\nu) g_{\mu\nu}. \quad (\text{B.36})$$

The Christoffel symbols here are defined via the metric function

$$\Gamma_{jk}^i = \frac{1}{2} g^{im} \left(\frac{\partial g_{mj}}{\partial x^k} + \frac{\partial g_{mk}}{\partial x^j} - \frac{\partial g_{jk}}{\partial x^m} \right). \quad (\text{B.37})$$

From here it follows

$$\Gamma_{tt}^t = \frac{1}{2} g^{tm} \left(\frac{\partial g_{mt}}{\partial t} + \frac{\partial g_{mt}}{\partial t} - \frac{\partial g_{tt}}{\partial x^m} \right). \quad (\text{B.38})$$

Due to the fact that only g_{tt} , g_{zz} , $g_{\rho\rho} \neq 0$ the equation above reduces to

$$\begin{aligned} \Gamma_{tt}^t &= \frac{1}{2} g^{tt} \left(\frac{\partial g_{tt}}{\partial t} + \frac{\partial g_{tt}}{\partial t} - \frac{\partial g_{tt}}{\partial t} \right) \\ &= \frac{1}{2} g^{tt} \frac{\partial g_{tt}}{\partial t}. \end{aligned} \quad (\text{B.39})$$

With $g_{tt} = \frac{1}{g^{tt}}$ the result is confirmed. The next Christoffel symbol is

$$\begin{aligned}
\Gamma_{\rho\rho}^t &= \frac{1}{2}g^{tm} \left(\frac{\partial g_{m\rho}}{\partial \rho} + \frac{\partial g_{m\rho}}{\partial \rho} - \frac{\partial g_{\rho\rho}}{\partial x^m} \right) \\
&= \frac{1}{2}g^{tt} \left(\frac{\partial g_{t\rho}}{\partial \rho} + \frac{\partial g_{t\rho}}{\partial \rho} - \frac{\partial g_{\rho\rho}}{\partial t} \right) \\
&= -\frac{1}{2}g^{tt} \frac{\partial g_{\rho\rho}}{\partial t}.
\end{aligned} \tag{B.40}$$

From the line element is clear that $g_{\rho\rho} = X^{2/3}$, which gives

$$\Gamma_{\rho\rho}^t = -\frac{1}{2}g^{tt} \frac{\partial}{\partial t} X^{2/3} = -\frac{1}{3}g^{tt} X^{-1/3} \frac{\partial X}{\partial t} = -\frac{1}{3} \frac{1}{g_{tt}} X^{-1/3} \frac{\partial X}{\partial t}. \tag{B.41}$$

The result we obtained using the variation of the action $\Gamma_{\rho\rho}^t = -\frac{1}{3} \frac{\partial X}{\partial t} \frac{1}{g_{tt}} X^{-1/3}$ agrees with this result. Now let us calculate Γ_{tz}^t

$$\begin{aligned}
\Gamma_{tz}^t &= \frac{1}{2}g^{tm} \left(\frac{\partial g_{mt}}{\partial z} + \frac{\partial g_{mz}}{\partial t} - \frac{\partial g_{tz}}{\partial x^m} \right) \\
&= \frac{1}{2}g^{tt} \left(\frac{\partial g_{tt}}{\partial z} + \frac{\partial g_{tz}}{\partial t} - \frac{\partial g_{tz}}{\partial t} \right) \\
&= \frac{1}{2}g^{tt} \frac{\partial g_{tt}}{\partial z} \\
&= \frac{1}{2} \frac{1}{g_{tt}} \frac{\partial g_{tt}}{\partial z}.
\end{aligned} \tag{B.42}$$

Finally we compute

$$\begin{aligned}
\Gamma_{t\rho}^t &= \frac{1}{2}g^{tm} \left(\frac{\partial g_{mt}}{\partial \rho} + \frac{\partial g_{m\rho}}{\partial t} - \frac{\partial g_{t\rho}}{\partial x^m} \right) \\
&= \frac{1}{2}g^{tt} \left(\frac{\partial g_{tt}}{\partial \rho} + \frac{\partial g_{t\rho}}{\partial t} - \frac{\partial g_{t\rho}}{\partial t} \right) \\
&= \frac{1}{2}g^{tt} \frac{\partial g_{tt}}{\partial \rho} \\
&= \frac{1}{2} \frac{1}{g_{tt}} \frac{\partial g_{tt}}{\partial \rho}.
\end{aligned} \tag{B.43}$$

The Christoffel symbols for the z coordinate also agree with the ones calculated

B PARAMETRISING THE SPHERICAL REGION

from the variation. Lastly for the ρ coordinate

$$\begin{aligned}
\Gamma_{\rho t}^{\rho} &= \frac{1}{2} g^{\rho m} \left(\frac{\partial g_{m\rho}}{\partial t} + \frac{\partial g_{mt}}{\partial \rho} - \frac{\partial g_{\rho t}}{\partial x^m} \right) \\
&= \frac{1}{2} g^{\rho\rho} \left(\frac{\partial g_{\rho\rho}}{\partial t} + \frac{\partial g_{\rho t}}{\partial \rho} - \frac{\partial g_{\rho t}}{\partial \rho} \right) \\
&= \frac{1}{2} g^{\rho\rho} \frac{\partial g_{\rho\rho}}{\partial t} \\
&= \frac{1}{2} X^{-2/3} \frac{\partial X^{2/3}}{\partial t} \\
&= \frac{1}{2} X^{-2/3} \frac{2}{3} X^{-1/3} \frac{\partial X}{\partial t} \\
&= \frac{1}{3} \frac{1}{x} \frac{\partial X}{\partial t},
\end{aligned} \tag{B.44}$$

and

$$\begin{aligned}
\Gamma_{\rho z}^{\rho} &= \frac{1}{2} g^{\rho m} \left(\frac{\partial g_{m\rho}}{\partial z} + \frac{\partial g_{mz}}{\partial \rho} - \frac{\partial g_{\rho z}}{\partial x^m} \right) \\
&= \frac{1}{2} g^{\rho\rho} \left(\frac{\partial g_{\rho\rho}}{\partial z} + \frac{\partial g_{\rho z}}{\partial \rho} - \frac{\partial g_{\rho z}}{\partial \rho} \right) \\
&= \frac{1}{2} g^{\rho\rho} \frac{\partial g_{\rho\rho}}{\partial z} \\
&= \frac{1}{2} X^{-2/3} \frac{\partial X^{2/3}}{\partial z} \\
&= \frac{1}{2} X^{-2/3} \frac{2}{3} X^{-1/3} \frac{\partial X}{\partial z} \\
&= \frac{1}{3} \frac{1}{x} \frac{\partial X}{\partial z}.
\end{aligned} \tag{B.45}$$

The Christoffel symbols from the two approaches match.

REFERENCES

References

- [1] D Grumiller, C. Ecker, and Stricker S. Evolution of the holographic entanglement entropy in an anisotropic system.
- [2] Philipp Stanzer. Holographic entanglement entropy in heavy ion collisions. Master's thesis (Diplomarbeit), Vienna University of Technology, Vienna, Austria, April 2016.
- [3] Shinsei Ryu and Tadashi Takayanagi. Aspects of holographic entanglement entropy. *JHEP*, 0608:045, 2006.
- [4] Pasquale Calabrese and John L. Cardy. Entanglement entropy and quantum field theory. *J.Stat.Mech.*, 0406:P06002, 2004.
- [5] Shinsei Ryu and Tadashi Takayanagi. Holographic derivation of entanglement entropy from ads/cft. *Phys.Rev.Lett.*, 96:181602, 2006.
- [6] Cern Courier. Alice enters new territory in heavy-ion collisions, 2011.
- [7] Jorge Casalderrey-Solana, Hong Liu, David Mateos, Krishna Rajagopal, and Urs Achim Wiedemann. Gauge/String Duality, Hot QCD and Heavy Ion Collisions. 2011.
- [8] Jorge Casalderrey-Solana, Hong Liu, David Mateos, Krishna Rajagopal, and Urs Achim Wiedemann. *Gauge/string duality, hot QCD and heavy ion collisions*. Cambridge: Cambridge University Press. vi, 2014.
- [9] Wilke van der Schee. *Gravitational collisions and the quark-gluon plasma*. PhD thesis, Utrecht U., 2014.
- [10] A. K. Chaudhuri. A short course on Relativistic Heavy Ion Collisions. 2012.
- [11] Mauricio Martinez and Michael Strickland. Measuring QGP thermalization time with dileptons. *Phys. Rev. Lett.*, 100:102301, 2008.
- [12] Inha University Nuclear Physics Experiment & Theory Group, Department of Physics. High-energy nuclear physics.
- [13] Gerard 't Hooft. A Planar Diagram Theory for Strong Interactions. *Nucl. Phys.*, B72:461, 1974.
- [14] Leonard Susskind. The World as a hologram. *J. Math. Phys.*, 36:6377–6396, 1995.
- [15] Juan Martin Maldacena. The large n limit of superconformal field theories and supergravity. *Int.J.Theor.Phys.*, 38:1113–1133, 1999.
- [16] S. W. Hawking. Information loss in black holes. *Phys. Rev.*, D72:084013, 2005.
- [17] Sean A. Hartnoll. Lectures on holographic methods for condensed matter physics. *Class. Quant. Grav.*, 26:224002, 2009.

- [18] G. Policastro, Dan T. Son, and Andrei O. Starinets. The Shear viscosity of strongly coupled $N=4$ supersymmetric Yang-Mills plasma. *Phys. Rev. Lett.*, 87:081601, 2001.
- [19] Veronika E. Hubeny, Mukund Rangamani, and Tadashi Takayanagi. A covariant holographic entanglement entropy proposal. *JHEP*, 0707:062, 2007.
- [20] Aitor Lewkowycz and Juan Maldacena. Generalized gravitational entropy. *JHEP*, 1308:090, 2013.
- [21] Arjun Bagchi, Rudranil Basu, Daniel Grumiller, and Max Riegler. Entanglement entropy in galilean conformal field theories and flat holography. *Phys.Rev.Lett.*, 114(11):111602, 2015.
- [22] Mark Srednicki. Entropy and area. *Phys. Rev. Lett.*, 71:666–669, 1993.
- [23] Paul M. Chesler and Laurence G. Yaffe. Horizon formation and far-from-equilibrium isotropization in supersymmetric Yang-Mills plasma. *Phys. Rev. Lett.*, 102:211601, 2009.
- [24] Paul M. Chesler and Laurence G. Yaffe. Boost invariant flow, black hole formation, and far-from-equilibrium dynamics in $N = 4$ supersymmetric Yang-Mills theory. *Phys. Rev.*, D82:026006, 2010.
- [25] Paul M. Chesler and Laurence G. Yaffe. Numerical solution of gravitational dynamics in asymptotically anti-de Sitter spacetimes. *JHEP*, 07:086, 2014.
- [26] Marco Cavaglia. Two-dimensional dilaton gravity. *AIP Conf. Proc.*, 453:442–448, 1998. [,442(1998)].
- [27] Ognen Kapetanoski. Anisotropy and dimensional reduction. May 2015.
- [28] Miguel Alcubierre. The Status of numerical relativity. pages 3–22, 2004.
- [29] Jeffrey Winicour. Characteristic evolution and matching. *Living Reviews in Relativity*, 15(2), 2012.
- [30] Ericourgoulhon. 3+1 formalism and bases of numerical relativity. 2007.
- [31] Michal P. Heller, David Mateos, Wilke van der Schee, and Diego Trancanelli. Strong Coupling Isotropization of Non-Abelian Plasmas Simplified. *Phys. Rev. Lett.*, 108:191601, 2012.
- [32] Michal P. Heller, David Mateos, Wilke van der Schee, and Miquel Triana. Holographic isotropization linearized. *JHEP*, 09:026, 2013.
- [33] Sebastian de Haro, Sergey N. Solodukhin, and Kostas Skenderis. Holographic reconstruction of space-time and renormalization in the AdS / CFT correspondence. *Commun. Math. Phys.*, 217:595–622, 2001.

REFERENCES

- [34] Charles Fefferman and C. Robin Graham. Conformal invariants. *Astérisque*, (Numero Hors Serie):95, 1985. The mathematical heritage of Élie Cartan (Lyon, 1984).
- [35] Vijay Balasubramanian and Simon F. Ross. Holographic particle detection. *Phys. Rev.*, D61:044007, 2000.
- [36] Guido Festuccia and Hong Liu. Excursions beyond the horizon: Black hole singularities in Yang-Mills theories. I. *JHEP*, 04:044, 2006.
- [37] Kenneth A. Brake. The surface evolver. May 1992.